EFFECT OF DIFFERENT PRESTRESSED FILM AND FILM-TENSIONING LINES ON THE CONTACT FORCE OF FLAT-ELLIPTICAL PIPE GREENHOUSES

/

不同预应力棚膜及压膜线对平椭圆管塑料大棚棚膜接触力的影响

Cunxing WEI [1)], Hengyan XIE [2,*)], Xin ZHENG [2)], Wenbao XU [2)]

[1)] College of Engineering, Heilongjiang Bayi Agricultural University, Daqing 163319

[2)] College of Civil Engineering and Water Conservancy, Heilongjiang Bayi Agricultural University, Daqing 163319;

Tel: +86-459-13766785587; E-mail: xiehy555@byau.cn

Corresponding author: Hengyan Xie

DOI: https://doi.org/10.35633/inmateh-77-20

Keywords: *flat-elliptical pipe greenhouse; contact model; sliding and sticking; fluctuating wind; wind-induced vibration responses*

ABSTRACT

This study utilized ABAQUS finite element software to model a flat-elliptical pipe greenhouse, focusing on the contact interactions among the greenhouse film, structural frame, and film-tensioning lines. A nonlinear finite element method was employed to investigate variations in contact pressure and shear stress under different prestress conditions of the greenhouse film and film-tensioning lines. The results showed that increasing the prestress of the greenhouse film increased contact pressure but decreased shear stress, whereas increasing the prestress of the film-tensioning lines raised both contact pressure and shear stress. Optimizing the combined prestress of the greenhouse film and film-tensioning lines can enhance the mechanical performance and wind resistance of the greenhouse structure.

摘要

本研究利用 ABAQUS 有限元软件对平椭圆管塑料大棚进行建模，重点分析棚膜、骨架和压膜线之间的接触作用。通过非线性有限元方法，研究了不同棚膜和压膜线预应力条件下接触压力与剪应力的变化规律。结果表明，棚膜预应力增大时，接触压力增大，接触剪应力减小；压膜线预应力增大时，接触压力和剪应力均增大。合理调整棚膜和压膜线的预应力组合，有助于优化棚膜结构的力学性能和抗风能力。

INTRODUCTION

Plastic greenhouses, as key production facilities in modern agriculture, are widely used in protective cultivation of vegetables, flowers, and fruit trees due to their lightweight structure, low cost, and excellent thermal insulation properties. Meanwhile, solar greenhouses influence the photosynthetic activity of fruits such as strawberries by regulating the internal temperature *(Cheng, 2023)*. However, in recent years, extreme climatic events have become more frequent, with strong winds, heavy snow, and other severe weather conditions often leading to greenhouse collapses, resulting in significant economic losses for agricultural production *(Briassoulis, 2016; Uematsu, 2020)*. As a result, the safety of greenhouse structures has increasingly become a focal point in agricultural engineering, and in-depth research and exploration are urgently needed to enhance the stability and safety of greenhouses under extreme weather conditions.

Existing research primarily focuses on the stability analysis of greenhouse frame structures and the investigation of their load-bearing capacity limits. For example, *Ren (2019)* used finite element analysis to develop a 20 m span plastic greenhouse frame model and performed loading analysis based on relevant specifications in China and Europe for typical loads. The study indicated that the greenhouse frame is particularly sensitive to the combined effects of static wind loads and non-uniform snow loads, and its structural safety is mainly influenced by both strength and stiffness.

Cunxing Wei, Ph.D. Eng.; Hengyan Xie, Prof. Ph.D. Eng.; Xin Zheng, Prof. Ph.D. Eng.; Wenbao Xu, Ph.D. Eng.

Similarly, researchers such as *Jiang (2021)*, *Wang (2022,2023),* and *Li (2022)* have studied the wind-induced responses of different types of greenhouse structural frames under fluctuating wind loads, exploring the effects of fluctuating wind on the structural safety of greenhouses, thereby enriching the theoretical system of wind-induced responses in greenhouse structures. In addition, *Xie (2025)* employed CFD simulations to investigate the impact of varying planting densities on the thermal and humid conditions within greenhouses, thereby contributing to the diversification of research methodologies for greenhouse environments under different conditions.

Most researchers have simplified wind loads as concentrated forces applied to the greenhouse frame, overlooking the more complex interactions between wind loads and the greenhouse structure in real-world applications. As research has progressed, scholars have gradually recognized that this simplification is significantly different from the actual situation. In reality, wind loads act directly on the greenhouse surface and are transmitted to the frame through the interaction between the film and the compression line. Consequently, some researchers have started to consider the greenhouse cover film as a crucial part of the overall structure and have carried out comprehensive force analyses, exploring the impact of different types of covering materials on the wind resistance of greenhouses. Previous studies have shown that the type of covering material significantly affects the wind resistance of greenhouses. For instance, *Qiao (2012)* investigated the wind resistance of an aluminum alloy greenhouse with an ETFE membrane roof, *Dougka (2020)* analyzed the wind resistance of a gothic greenhouse covering film, and *Ding (2013, 2016)* examined the wind resistance of the covering film, flat glass, and PC panels used in North China-type, Venlo-type, and sunlit greenhouses. These studies indicate that selecting appropriate covering materials can effectively improve the wind resistance of greenhouses.

Although existing research has provided theoretical support for the wind resistance of greenhouse structural frames and covering materials, the issue of film damage has not been sufficiently addressed. As a flexible structure, the greenhouse film exhibits considerable deformability and elasticity, making it prone to rupture, tearing, and other forms of damage under the effect of strong winds, particularly under extreme weather conditions where the stress state becomes unusually complex. Film's damage not only directly affects the stability of the internal environment of the greenhouse, but also may lead to crop production losses. In severe cases, it may even threaten the stability and profitability of the entire agricultural production system.

Through literature review and field investigations by our research group, the main causes of film damage can be categorized into two types: one is excessive prestress in the film, leading to deformation upon contact with the frame (as shown in Fig. 1(a)); the other is slippage between the film-tensioning line and the film, causing friction between the two (as shown in Fig. 1(b)). Under the cyclic action of wind loads, both factors can trigger damage to the film, thus impacting the overall wind resistance of the greenhouse. Therefore, it is of great academic value and practical significance to investigate the mechanical interactions between the film, frame, and film-tensioning line and to assess the impact of wind loads on film damage.

a) Contact between the film and frame ***b) Contact between the film and film-tensioning line***

Fig. 1 – Damage to film due to different types of contact forces

This study will focus on a novel 10 m span plastic greenhouse with a flat-elliptical pipe greenhouse (FEPG) in Northern China's cold regions. Using ABAQUS finite element software, the contact interactions between the film-tensioning line and the film, as well as between the film and the frame, are simulated, considering the effects of film prestress and film-tensioning line prestress. The aim is to systematically analyze the mechanical behavior of the film under wind loads. This study seeks to fill the gap in the theory of wind-induced responses in plastic greenhouses, particularly in terms of film prestress and film-tensioning line prestress, and to further improve the theoretical frame for wind-induced responses in greenhouses, providing more scientific modeling methods and design bases for wind resistance design in greenhouse structures.

MATERIALS AND METHODS

Contact equilibrium equation and solution method

There are several computational methods available for the analysis of wind-induced vibrations in membrane structures. Among these, three primary approaches are widely recognized and extensively applied: the force density method, the nonlinear finite element method (FEM), and the dynamic relaxation method. The nonlinear FEM involves discretizing the membrane structure into finite elements, allowing for high precision in computational results. This method is particularly suited for analyzing complex phenomena such as large deformations, material nonlinearity, and geometric nonlinearity. It is commonly employed in response analysis of membrane structures subjected to extreme loading conditions, such as wind forces. For this study, the nonlinear finite element method is selected as the primary approach for the subsequent analyses.

The fundamental governing equations for this method are as follows:

$$([K_L]+[K_{NL}])\{\Delta u\}=\{P\}\{F\} \tag{1}$$

where: $[K_L]$ is the linear stiffness matrix of the structure; $[K_{NL}]$ is the nonlinear stiffness matrix of the structure; $\{\Delta u\}$ is the displacement vector of the structure; $\{P\}$ is the load vector, and $\{F\}$ is the equivalent nodal force vector.

The normal force equilibrium equation for the film in the structure is as follows:

$$\frac{\partial T_x}{\partial x}+\frac{\partial T_y}{\partial y}+p_l+p_s=0 \tag{2}$$

where: T_x is the stress in the x-direction (along the length of the film) is generated by the stretching of the film, resulting in tensile stress in the positive direction; T_y is the stress in the y-direction (along the width of the film) is generated by the stretching of the film; p_l is the normal pressure between the film-tensioning line and the film arises due to the radial constraint exerted by the compression line on the film. p_s is the normal pressure between the film and the frame.

The tangential force equilibrium equation for the film in the structure is as follows:

$$\frac{\partial \tau_{xy}}{\partial x}+\frac{\partial \tau_{xy}}{\partial y}+\tau_l+\tau_s=0 \tag{3}$$

where: τ_{xy} is the shear stress on the film represents the tangential stress acting on the film surface; τ_l is the shear stress between the film-tensioning line and the film; τ_s is the shear stress between the film and the frame.

Finite element model

Material parameter

In this study, the frame is constructed from Q235B galvanized steel pipes, which offer superior strength, rigidity, and corrosion resistance. The greenhouse film utilized is polyolefin (PO) film, a material widely employed in practical engineering applications. This film not only demonstrates exceptional toughness and ductility but also exhibits significant advantages in terms of light transmittance, thermal insulation, and longevity. The film-tensioning line is primarily composed of polyamide, also known as nylon, a high-performance synthetic fiber renowned for its excellent wear resistance and elasticity. This material is capable of withstanding substantial tensile forces, making it well-suited for tension transmission within the greenhouse structure and ensuring the stability of the membrane. The material parameters for each component of the flat-elliptical pipe greenhouse are summarized in Table 1.

Table1

Material parameter of frame, film and film-tensioning line

Material	b×h or R (mm)	t (mm)	ρ (kg/m³)	f_y (MPa)	λ	E (MPa)
Rafter	30×60	2	7.85	235	0.28	2.1×105
Embedded steel pipe	30×80	2	7.85	235	0.28	2.1×105
Purlin	ϕ 20	2	7.85	235	0.28	2.1×105
Film	/	0.12	0.94	/	0.44	500
Film-tensioning line	20	2	1.15	/	0.35	3500

Contact modal building

In this study, a contact model was established using the ABAQUS finite element software. The structural frame was discretized using C3D8R solid elements, the greenhouse film was represented by M3D4R membrane elements, and the film-tensioning line was discretized using B31 beam elements.

The arch feet are welded to flat-elliptical pipe embedded along the longitudinal axis of the greenhouse and are further welded to ground anchors, forming a support system with substantial stiffness. In the ABAQUS model, the connection between the frame feet and the bottom steel pipes is defined as a fixed end, restricting both translational and rotational movements in all directions.

The contact pair definition follows the principle that the master surface is typically selected based on its higher rigidity and coarser mesh, while the slave surface is chosen based on its finer mesh. In this study, nodes on the frame are selected to establish point-to-surface contact pairs with the film surface. Similarly, nodes on the film-tensioning line are selected to establish point-to-surface contact pairs with the film surface, as illustrated in Fig. 2.

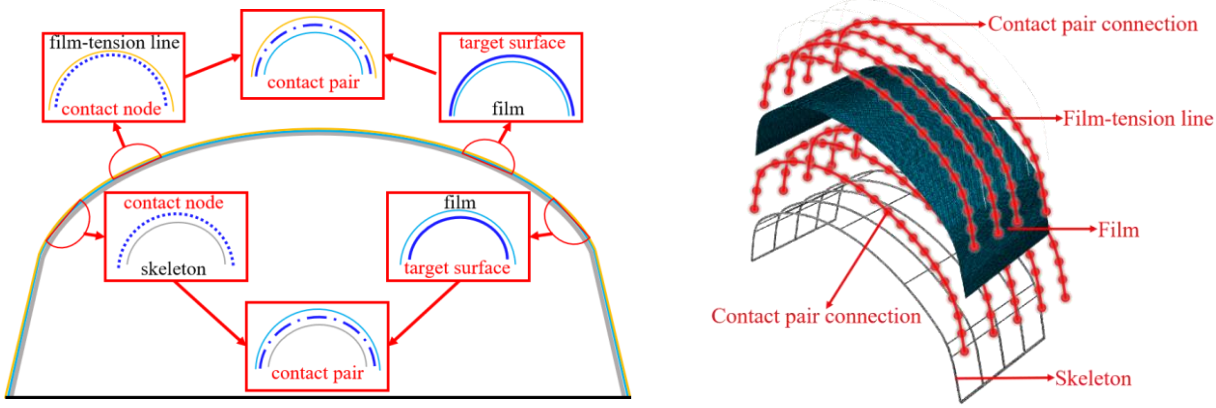

a) 2D combined display *b) 3D layered display*

Fig. 2 – Contact Pair

Wind load simulation and application

The plastic greenhouse analyzed in this study is located in Jiamusi City, Heilongjiang Province, China. According to the *Chinese standard GB/T50009-2012 (Mohued, 2012)*, the design service life of the plastic greenhouse is set at 10 years. Based on available tables, the basic wind pressure in Jiamusi is 0.38 kN/m², with the instantaneous wind speed corresponding to a 3-second gust used for calculation. Additionally, according to the *Chinese standard GB/T50009-2012 (Mohued, 2012)*, the basic wind pressure in Jiamusi is 0.65 kN/m², which is based on a 10-minute average wind speed for a 50-year return period. According to relevant literature, the ratio of wind pressure for a 10-year return period to that for a 50-year return period is 0.734. Thus, the 10-minute basic wind pressure for a 10-year return period can be calculated as follows:0.65×0.734=0.477 kN/m².
Considering the results from both codes, this study adopts a basic wind pressure value of 0.477 kN/m² for the analysis.

According to Bernoulli's equation in fluid mechanics, there exists a relationship between wind pressure and wind speed, expressed as follows:

$$w = \frac{1}{2}\rho v^2 = \frac{\gamma}{2g}v^2 \tag{4}$$

where w is wind pressure, kN/m², ρ is air density, kPa, v is wind speed, m/s, γ is air gravity density, kN/m³, g is gravitation acceleration, m/s².

In the above equation, the air gravity density ρ is 0.012018 kN/m³ at the standard atmospheric pressure of 101.235 kPa. Jiamusi is located near 45° north latitude, g=9.8m/s². Under these conditions, the wind pressure can be calculated by equation (1):

$$w = \frac{1}{2}\rho v^2 = \frac{0.012018}{2\times 9.8}v^2 = \frac{v^2}{1630} \tag{5}$$

Based on the relationship between wind pressure and wind speed, the average wind speed at a standard height of 10 meters under standard terrain type B conditions, considering a 10-year return period and a 10-minute interval, is calculated to be 27.88 m/s.

According to the *Chinese standard GB/T 51183-2016 (Mohued, 2016)*, the wind load acting on the main structure of the greenhouse, perpendicular to its surface, can be calculated using the following formula:

$$w_k = \mu_s \mu_z w \tag{6}$$

where w_k is the standard value of the wind load (kN/m²); μ_S is the shape coefficient of wind pressure shown in Fig.3; μ_Z is the wind pressure height variation coefficient; w is the wind pressure acting on structure (kN/m²), and here it is the full dynamic wind pressure.

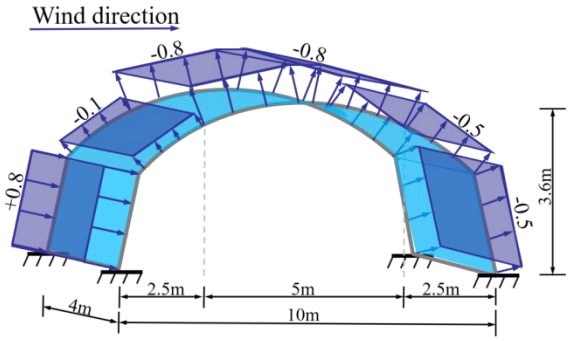

Fig. 3 – Shape coefficient on the flat-elliptical pipe frame plastic greenhouse film

This study applies wind loads in the form of surface pressure directly onto the film during the wind-induced response analysis. This approach ensures that the load remains consistently normal to the structure's surface throughout the analysis, thereby providing a more accurate representation of wind action and aligning more closely with the relevant design code specifications.

RESULTS AND DISCUSSION

Contact forces between the film and the frame

Contact shear stress

The contact shear stress between the film-tensioning line and the film under varying prestress conditions of the film (3 MPa, 4 MPa, 5 MPa, 6 MPa, 7 MPa) and different prestress conditions of the film-tensioning lines (5.5 MPa, 6.5 MPa, 7.5 MPa, 8.5 MPa, 9.5 MPa) is illustrated in Fig. 4.

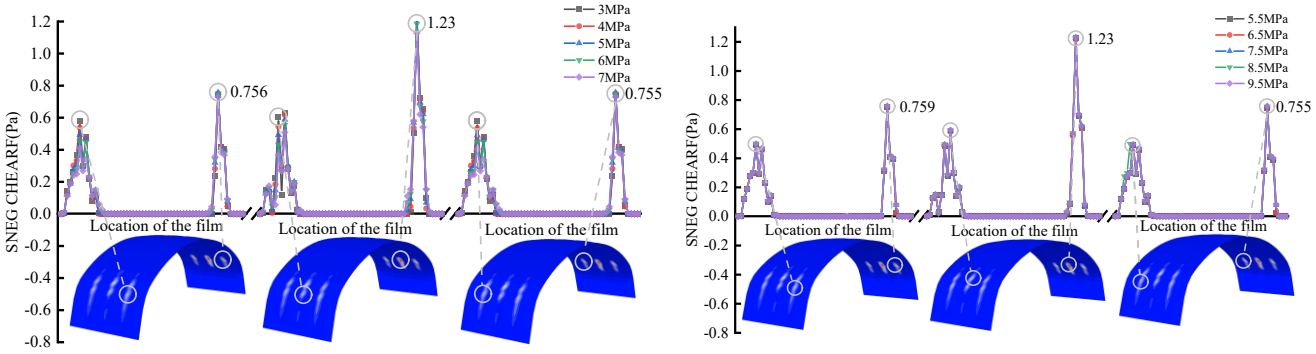

a) Different prestress of film *b) Different prestress of film-tensioning line*

Fig. 4 – Contact shear stress between the film and the frame

As illustrated in the figure, the contact shear stress between the frame and the film is primarily concentrated in the windward and leeward shoulder regions of the contact interface. This stress exhibits a bimodal and asymmetric distribution along the x-axis, while it displays an elongated, strip-like pattern along the y-axis. Specifically, the contact shear stress between the film and the central frame is significantly higher than that observed at the lateral frames. This phenomenon can be attributed to the boundary conditions applied in the model, where the film is assumed to be fixed to the frame at both ends, thus preventing relative displacement. This setup mimics practical engineering scenarios, where, near the ends, the film experiences limited bulging, restricting its relative movement to the frame. In contrast, the central region of the film undergoes more pronounced bulging under wind load, resulting in greater relative displacement and, consequently, higher contact shear stress.

As the prestress in the film increases, the contact shear stress on the windward side gradually decreases. This reduction is likely due to the increased surface tension of the film, which smoothens the surface and alters the frictional interaction between the film and the frame. When the film prestress reaches 3 MPa, the contact shear stress between the film and the central frame is 1.07 and 1.08 times greater than those at the lateral frames, respectively. This can be explained by the fact that the increased prestress strengthens the radial constraint between the film and the frame, thereby reducing relative displacement and lowering the shear stress. On the leeward side, the contact shear stress initially increases, then decreases, with rising film prestress. At a prestress of 5 MPa, the peak contact shear stress between the central frame and the film reaches 1.23 Pa, which is 1.626 and 1.628 times higher than the corresponding values at the lateral frames. However, at 7 MPa, the contact shear stress decreases by approximately 9.7% compared to the maximum value.

Conversely, the contact shear stress on the windward side increases with increasing prestress in the film-tensioning lines. This trend is likely attributed to the fact that higher prestress in the film-tensioning lines not only enhances the constraint effect between the film and the film-tensioning lines but also indirectly increases the radial constraint between the film and the frame. At a film-tensioning line prestress of 7 MPa, the peak contact shear stress on the windward side reaches 0.594 Pa, which is 1.19 and 1.20 times greater than that at the lateral frames, reflecting a 1.5% increase compared to the stress at a prestress of 3 MPa. Similarly, on the leeward side, when the film-tensioning line prestress reaches 7 MPa, the peak contact shear stress is 1.2301 Pa-1.62 and 1.621 times greater than at the lateral frames-representing a 0.41% increase compared to the stress at 3 MPa.

Contact pressure

The contact pressure between the film-tensioning line and the film under varying prestress conditions of the film and different prestress conditions of the film-tensioning lines is illustrated in Fig. 5.

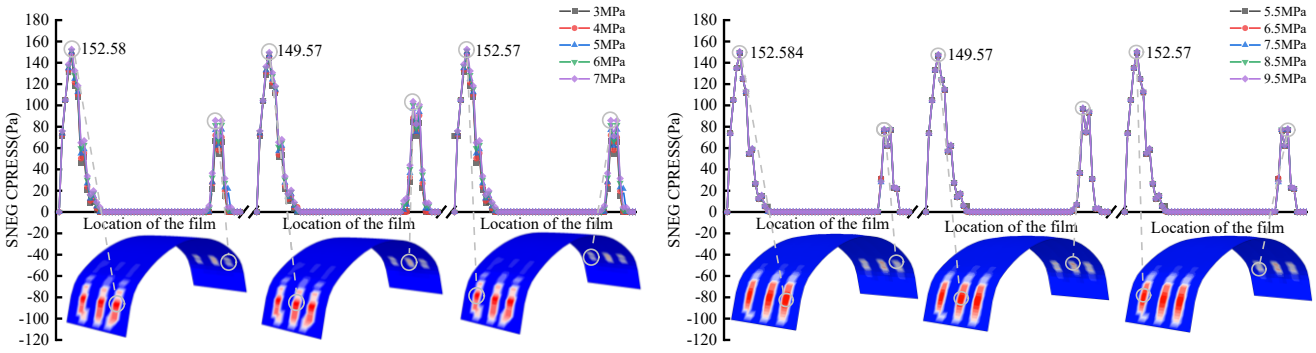

a) Different prestress of film *b) Different prestress of film-tensioning line*

Fig. 5 – Contact pressure between the film and the frame

As depicted in the figure, the contact pressure between the greenhouse film and the frame is primarily concentrated in the windward and leeward shoulder regions of their interface, displaying a block-like distribution along the y-axis. Under wind loading, the windward side, extending from the foot to the shoulder, bears the majority of the wind pressure, leading to direct contact between the film and the frame. In this context, the maximum contact pressure between the film and the central frame on the windward side is slightly lower than that observed at the two lateral frames. This phenomenon can be attributed to the bulging of the film from the windward foot toward the leeward shoulder under wind load, resulting in a more pronounced separation between the film and the central frame compared to the lateral frames. Simultaneously, the region from the windward shoulder to the leeward foot predominantly experiences suction forces. Since the direction of suction opposes that of the contact compressive stress, it effectively mitigates the contact pressure between the film and the frame on the leeward side.

As the prestress in the film increases, the contact pressures on both the windward and leeward sides rise. This is due to the increased tension in the film as prestress increases, which alters the deformation of the film and, consequently, strengthens the radial constraint exerted by the film on the frame, leading to elevated contact pressures. On the windward side, variations in maximum contact pressure across different locations are minimal, with the peak contact pressure occurring at the interface between the film and the first frame. When the film prestress reaches 7 MPa, the maximum contact pressure reaches 152.58 Pa, representing a 3.4% increase compared to the pressure at 3 MPa prestress. On the leeward side, the maximum contact pressure between the film and the central frame is 103.6 Pa, which is 1.206 and 1.207 times greater than the pressures at the lateral frames, respectively, indicating a 22.6% increase relative to the 3 MPa prestress condition.

Moreover, increasing the prestress of the film-tensioning lines similarly leads to higher contact pressures on both the windward and leeward sides. This is due to the enhanced radial constraint exerted by the increased prestress in the tensioning lines on the film, thereby increasing the contact pressure between the film-tensioning lines and the film, as well as between the film and the frame. On the windward side, variations in maximum contact pressure across positions are minimal, with the peak pressure again occurring at the first frame-film interface. At a film-tensioning line prestress of 9.5 MPa, the maximum contact pressure reaches 150.25 Pa, reflecting a 0.5% increase compared to the value at 5.5 MPa film prestress. On the leeward side, the peak contact pressure between the membrane and the central arch frame is 97.5 Pa, which is 1.24 and 1.25 times higher than the contact pressures at the lateral frames under the same film-tensioning line prestress condition, representing a 1.06% increase compared to the 3 MPa prestress scenario.

Contact forces between the film and the film-tensioning line

Contact shear stress

The contact shear stress between the film-tensioning line and the film under varying prestress conditions of the film and different prestress conditions of the film-tensioning lines is illustrated in Fig. 6.

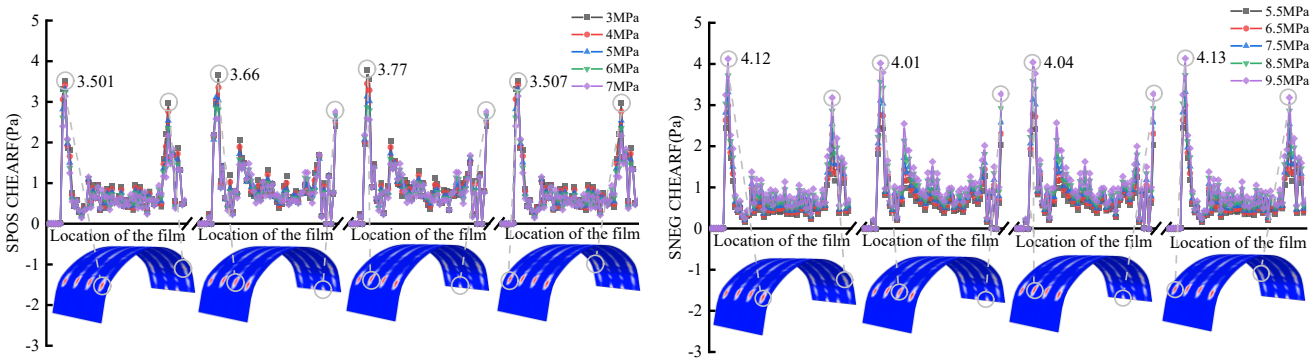

a) Different prestress of film ***b) Different prestress of film-tensioning line***

Fig. 6 – Contact shear stress between the film and the film-tensioning line

As illustrated in the figure, the contact shear stress between the film-tensioning lines and the greenhouse film is primarily concentrated in the region from the windward shoulder to the leeward shoulder, where the film and the tensioning lines come into contact. This stress exhibits a bimodal, asymmetric distribution along the x-axis and a strip-like distribution along the y-axis.

Under varying prestress conditions of the film, the maximum contact shear stress between the two central film-tensioning lines and the film is significantly higher than that observed between the film and the other two lateral film-tensioning lines. This phenomenon can be attributed to the boundary conditions applied in the model, where the film is assumed to be fixed at both ends to the frame, preventing relative displacement. This configuration is designed to more accurately simulate practical engineering scenarios. Due to the limited bulging of the film near the two end frames, relative motion between the film and the film-tensioning lines is constrained. In contrast, the contact region between the central two film-tensioning lines and the film experiences more pronounced relative movement, leading to higher contact shear stress.

Additionally, under different prestress conditions of the film-tensioning lines, the maximum contact shear stress between the two central film-tensioning lines and the film is notably lower than that between the lateral film-tensioning lines and the film. This observation further validates the role of the film-tensioning lines in regulating the wind pressure distribution on the surface of the film. By altering the wind pressure distribution on the film's surface, the film-tensioning lines effectively mitigate the excessive concentration of wind pressure, resulting in a more uniform and reasonable distribution.

As the prestress in the film increases, the contact shear stress on the windward side decreases. This reduction may be due to the increased film prestress, which enhances the film's surface tension, smooths the film surface, and alters the friction coefficient between the film and the tensioning lines. The peak contact shear stress on the windward side occurs at the third film-tensioning line position. At a film prestress of 3 MPa, the contact shear stress between the third tensioning line and the film is 1.07, 1.03, and 1.13 times higher than those between the film and the other film-tensioning lines, respectively. When the film prestress increases to 7 MPa, the peak contact shear stress decreases by 31.29%.

As the prestress of the compression line increases, the contact shear stress on both the windward and leeward sides also increase. This may be due to the fact that the increase in prestress not only enhances the constraint between the compression line and the membrane but also indirectly strengthens the radial restraining force between the membrane and the framework.

When the prestress of the compression line is 7 MPa, the peak contact shear stress on the windward side occurs at the region where the fourth compression line contacts the membrane, with a value of 4.13 Pa.

This value is 1.002 times, 1.028 times, and 1.024 times that of the peak contact shear stresses of the other compression lines. Compared to the scenario when the prestress is 3 MPa, the contact shear stress increases by 55.26%. On the leeward side, when the prestress of the compression line is 7 MPa, the peak contact shear stress occurs at the region where the third compression line contacts the membrane, with a value of 3.267 Pa. This represents a 60.5% increase in contact shear stress compared to when the prestress is 3 MPa.

Contact pressure

The contact pressure between the film-tensioning line and the film under varying prestress conditions of the film and different prestress conditions of the film-tensioning lines is illustrated in Fig. 7.

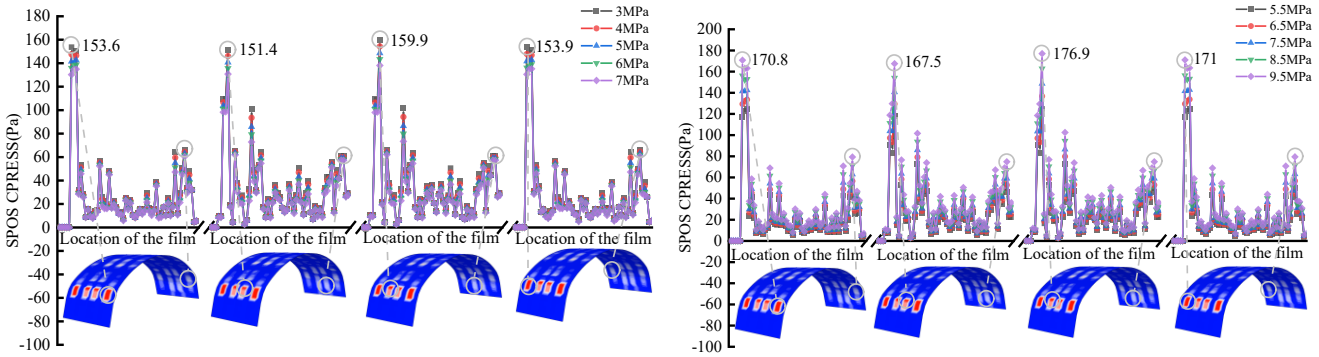

a) Different prestress of film *b) Different prestress of film-tensioning line*

Fig. 7 – Contact pressure between the film and the film-tensioning line

As illustrated in the figure, the contact pressure between the film-tensioning line and the film is primarily distributed from the windward shoulder to the leeward shoulder region, where the frame contacts the film, exhibiting a block-like distribution along the y-axis. Under wind loading, the windward side, from the foot to the shoulder of the film, may experience separation between the film-tensioning line and the film due to wind pressure, resulting in a lack of contact pressure in this region. Conversely, from the windward shoulder to the leeward bottom, the film is subjected to suction forces, which cause it to bulge outward. At this point, the film-tensioning line exerts radial restraint on the film, leading to significant contact pressure between the two components.

Under varying prestress conditions of both the film and the film-tensioning line, the trends in contact pressure at the cable ends remain generally consistent and numerically close. However, although the two central film-tensioning lines exhibit similar trends in the variation of contact pressure with the film, their magnitudes differ considerably. This phenomenon can be attributed to the bulging of the film from the windward foot to the leeward shoulder under wind load, which is constrained by the film-tensioning lines, limiting excessive deformation of the film. Moreover, the film-tensioning lines influence the distribution of wind pressure on the film surface, which further contributes to variations in contact pressure.

As the prestress in the film increases, contact pressures on both the windward and leeward sides decrease. This is due to the increased tension in the film as prestress rises, which alters its deformation characteristics and strengthens the radial restraint exerted by the film on the frame, ultimately reducing the contact pressure. On the windward side, the peak contact pressure between the film-tensioning line and the film occurs at the third film-tensioning line position. When the film prestress is 3 MPa, the peak contact pressure is 159.9 Pa, which is 1.04, 1.05, and 1.03 times the values at the other film-tensioning line positions, respectively. When the film prestress increases to 7 MPa, the contact pressure decreases to 138.1 Pa, representing a 13.6% reduction. On the leeward side, the differences in maximum contact pressure among the film-tensioning lines are minimal, with the peak occurring at the fourth frame position in contact with the film. At 3 MPa film prestress, the maximum contact pressure is 65.92 Pa, decreasing to 60.49 Pa (an 8.23% reduction) at 7 MPa prestress.

With increasing prestress in the film-tensioning lines, contact pressures on both the windward and leeward sides increase. This can be attributed to the enhanced radial restraint exerted by the film-tensioning lines on the film, which leads to elevated contact pressures between the two.

The peak contact pressure on the windward side occurs at the fourth film-tensioning line position, reaching 171.06 Pa at a 9.5 MPa film-tensioning line prestress—an increase of 45.7% compared to the 5.5 MPa prestress condition. On the leeward side, the peak contact pressure also occurs at the fourth film-tensioning line position, reaching 79.43 Pa at 9.5 MPa, which is 1.002, 1.15, and 1.15 times the contact pressures at the other film-tensioning line positions, respectively, representing a 58.22% increase compared to the 3 MPa film-tensioning line prestress condition.

CONCLUSIONS

In this study, the ABAQUS finite element software was used to model the elliptical plastic greenhouse, with a focus on the contact interactions between the greenhouse film, frame, and film-tensioning line. A systematic analysis based on nonlinear finite element methods was conducted to investigate the variations in contact pressure and contact shear stress between the film, frame, and film-tensioning lines. Under different prestress conditions of the greenhouse film and film-tensioning lines. The main findings are as follows:

(1) As the prestress of the greenhouse film increased, the contact pressure between the film and the frame, as well as between the film and the film-tensioning lines, also increased. This is due to the increased tension in the film as the prestress was elevated, which altered the deformation of the film and enhanced its radial constraint on the frame, thus resulting in higher contact pressure between the two.

(2) As the prestress of the greenhouse film increased, the contact shear stress between the film and the frame, as well as between the film and the film-tensioning lines, decreased. This can be attributed to the increase in tension on the film surface, which improved its smoothness and modified the friction coefficient between the film and the frame, leading to a reduction in the contact shear stress.

(3) As the prestress of the film-tensioning lines increased, the contact pressure between the film and the frame, as well as between the film and the film-tensioning lines, increased. This is because the prestress in the film-tensioning lines enhanced their radial constraint on the film, thereby increasing the contact pressure between the film-tensioning lines and the film, as well as between the film and the frame.

(4) As the prestress of the tensioning lines increased, the contact shear stress between the film and the frame, as well as between the film and the film-tensioning lines, increased. This is primarily due to the enhanced constraint effect of the film-tensioning lines on the film, which indirectly increased the radial constraint force between the film and the frame.

The study suggests that optimizing the combination of prestress in the film and film-tensioning lines is essential for improving the mechanical performance and wind resistance of the greenhouse structure. Future work could explore the nonlinear properties of film materials and dynamic wind load effects to further enhance design predictions and the resilience of greenhouse film structures under extreme weather conditions.

ACKNOWLEDGEMENTS

This study is supported by Natural Science Foundation of Heilongjiang Province of China (LH2019E072). All authors are grateful for this support.

REFERENCES

[1] Briassoulis. D., Dougka, G., Dimakogianni, D., & Vayas, I. (2016). Analysis of the collapse of a greenhouse with vaulted roof. *Biosystems Engineering*, Vol.151, pp. 495-509, England. DOI: https://doi.org/10.1016/j.biosystemseng.2016.10.018

[2] Cheng W., Wang Y., Wang C., Wang T., He J., Liu Z., Xu Y., (2023). Study on the variation of thermal environment and photosynthesis characteristics of strawberry in a solar greenhouse, *INMATEH - Agricultural Engineering*, Vol. 70, pp. 211-220, Bucharest/Romania. DOI: https://doi.org/10.35633/inmateh-70-21

[3] Ding, M., Shi, X., Li, M., Ju, J., & Jiang, X. (2013). Load-bearing capacity of films and its effect on structure stability of Chinese solar greenhouse (薄膜承载力及其对日光温室结构稳定性能的影响). *Transactions of the Chinese Society of Agricultural Engineering*, Vol. 29, No. 12, pp. 194-202, Beijing/China. DOI: https:/doi.org/10.3969/j.issn.1002-6819.2013.12.025

[4] Ding, M., Li, M., Shi, X., Zhang, P., & Jiang, X. (2016). Stable bearing capacity calculation of greenhouse structures considering skin effect of covering material (考虑覆盖材料蒙皮效应的温室结构稳定承载力计算). *Transactions of the Chinese Society of Agricultural Engineering*, Vol. 32, No. 1, pp. 224-232, Beijing/China. DOI: https://doi.org/10.11975/j.issn.1002-6819.2016.z1.031

[5] Dougka, G, Briassoulis. D. (2020). Load carrying capacity of greenhouse covering films under wind action: Optimising the supporting systems of greenhouse films. *Biosystems Engineering,* Vol. 192, pp, 199 -214, England. DOI: https://doi.org/10.1016/j.biosystemseng.2020.01.020

[6] Jiang Y., Bai Y., Wang C., Wang Y., Pang X. (2021). Dynamic response analyses of plastic greenhouse structure considering fluctuating wind Load. *Advances in Civil Engineering*. Vol. 2021, pp. 1-13, Egypt. DOI: https://doi.org/10.1155/2021/8886557

[7] Li, X., Wang C., Jiang Y., Bai, Y. (2022). Dynamic response analysis of a whole steel frame solar greenhouse under wind loads. *Scientific reports*. Vol. 12, pp. 1-12, England. DOI: https://doi.org/10.1038/s41598-022-09248-z

[8] MOHURD. (2012). *GB 50009-2012 Load code for the design of building structures.* (建筑结构荷载规范). Beijing, China: China Architecture & Building Press (in Chinese). DOI: https://www.mohurd.gov.cn/gongkai/fdzdgknr/tzgg/201207/20120723_210754.html.

[9] MOHURD. (2016). *GB/T 51183-2016 Code for the design load of horticultural greenhouse structures*. （农业温室结构荷载规范）. Beijing, China: China Planning Press (in Chinese) https://www.mohurd.gov.cn/gongkai/zhengce/zhengcefilelib/201702/20170214_230578.html.

[10] Qiao, K., Wu, M., Zhang, Q. (2012). Analysis on wind resistance performance of ETFE membrane roof in aluminum alloy greenhouse (铝合金温室拱形 ETFE 膜屋面抗风性能分析). *Transactions of the Chinese Society of Agricultural Engineering*. Vol. 28, No. 14, pp. 170-176, Beijing/China. DOI: https://doi.org/10.3969/j.issn.1002-6819.2012.14.026

[11] Ren, J., Wang, J., Guo, S., Li, X., Zheng, K., & Zhao, Z. (2019). Finite element analysis of the static properties and stability of a large-span plastic greenhouse. *Computers and Electronics in Agriculture.* Vol. 165, pp. 1-9, England. DOI: https://doi.org/10.1016/j.compag.2019.104957

[12] Uematsu, Y., & Takahashi, K. (2020). Collapse and reinforcement of pipe-framed greenhouse under static wind loading. *Journal of Civil Engineering and Architecture*, Vol. 14, pp. 583-594, United States. DOI: https://doi.org/10.17265/1934-7359/2020.11.001

[13] Wang, C., Jiang, Y., Wang, T., Xu Z., Bai, Y. (2022). Analysis of wind-induced responses of landing assembled Chinese solar greenhouses. *Biosystems Engineering*, Vol. 220, No. 6, pp. 214-232, England. DOI: https://doi.org/10.1016/j.biosystemseng.2022.06.003

[14] Wang, C., Xu Z., Jiang, Y., Bai, Y., & Wang, T., (2023). Numerical analysis of static and dynamic characteristics of large-span pipe-framed plastic greenhouses. *Biosystems Engineering*, Vol. 232, No. 6, pp. 67-80, England. DOI: https://doi.org/10.1016/j.biosystemseng.2023.06.013

[15] Xie Q., Ren J., (2025). Research on greenhouse planting density of landscape flowers in cold regions based on CFD simulation, *INMATEH - Agricultural Engineering*, Vol. 75, No. 1, pp. 469-479, Bucharest/Romania. DOI: https://doi.org/10.35633/inmateh-75-40